22nd International Conference on Sustainable Energy Technologies
Kuala Lumpur, Malaysia, 13 to 15 August 2026 · ISBN 978-1-995850-00-9 · ISSN 2978-4387

CONFERENCE PAPER · ENERGY STORAGE & CONVERSION

Numerical analysis of support columns in vapor chambers

Haojiang Ran[1], Xinyi Wang[1], Lu Wang[1], Tiexiao Xu[1], Zhen Li[1]*

[1] Key Laboratory for Thermal Science and Power Engineering of Ministry of Education, Department of Engineering Mechanics, Tsinghua University, Beijing, China

RECEIVED 30 May 2026 · REVISED 30 June 2026 · ACCEPTED 7 July 2026
PRESENTED 13 to 15 August 2026 · PUBLISHED 23 November 2026

ABSTRACT

Vapor chambers (VCs) were widely used as passive heat spreaders for the thermal management of chips, batteries, and electronic devices. Support columns were incorporated to maintain mechanical stability, enhance heat conduction, and provide liquid-return pathways. However, the support columns also affected the vapor-flow field and obstructed vapor transport. In this work, the authors developed and assessed a transient numerical model to investigate the thermal-hydraulic performance of vapor chambers with different support-column configurations. An equivalent thermal conductivity method was first established to obtain an approximate temperature distribution. Subsequently, the liquid-vapor interface was modelled using a mass-transfer formulation based on local energy balance, the Clausius-Clapeyron relation, and kinetic theory. The proposed method was approximately 1.84 times faster than the conventional transient flow calculation and provided improved initialization and computational robustness. Vapor chambers with different support-column pitches were then compared. The effects of support-column pitch on thermal resistance, temperature uniformity, temperature distribution, and liquid and vapor pressure drops were analysed. The support columns introduced additional conductive heat-transfer paths while simultaneously redistributing the vapor flow and phase-change processes. As the number of support columns increased, the thermal resistance decreased, whereas the temperature non-uniformity and vapor pressure drop increased and the liquid pressure drop decreased. The results provided guidance for the design of vapor chambers for thermal-management applications.

KEYWORDS Vapor chambers, Thermal management, Support columns, Numerical method

1. Introduction

With the rapid development of artificial intelligence, the power consumption and heat dissipation of electronic devices had increased substantially, and nearly all electrical input power was ultimately converted into heat. Operation outside the allowable temperature range could directly impair device performance and reliability, which made effective thermal management increasingly important. A common thermal-management strategy was to spread heat through highly conductive solids and subsequently dissipate it by forced convection.

Vapor chambers, also known as flat heat pipes, had been widely used as efficient passive heat spreaders that transported heat primarily through liquid-vapor phase change. Compared with highly conductive solids, vapor chambers provided high effective in-plane thermal conductivity and good temperature uniformity. A typical vapor chamber consisted of enclosure walls, a wick, a vapor core, a working fluid, and support columns. Despite their widespread industrial use, the thermal-hydraulic characteristics inside vapor chambers had not yet been fully understood. Investigations of the internal transport processes had mainly relied on theoretical analysis, numerical simulation, and visualization experiments.

* Corresponding author. Email address: lizh@tsinghua.edu.cn (Zhen Li)

© 2026 The Author(s).
Published by Caravel Press.

doi.org/10.65582/set.2026.014

Numerical simulation had been widely used to reproduce the coupled physical processes in vapor chambers while reducing experimental cost and resource consumption. Prasher introduced a conduction-based model to assess the heat-transport capability of heat pipes and vapor chambers for various configurations. By combining theoretical analysis with experiments, an effective thermal conductivity for the vapor chamber was obtained, which substantially simplified the simulation and yielded good agreement with the experimental results. However, the method provided only an approximate temperature field and did not resolve the actual fluid-flow process (Prasher 2003). Koito et al. developed a steady-state mathematical model for three-dimensional vapor chambers and obtained the capillary-pressure head required to circulate the working fluid; large temperature drops were identified in the liquid-wick region and the solid wall near the heat source (Koito *et al.* 2006). Vadakkan et al. proposed a transient calculation method in which the system pressure was determined by the initial masses of vapor and liquid and was subsequently updated according to changes in the vapor mass caused by heat addition and phase change. The numerical results were in good agreement with the experimental data.

In this study, the authors proposed a two-stage sequential transient numerical model to analyse the performance of vapor chambers. The liquid-vapor interface was treated numerically as a wall, and interfacial heat and mass transfer were implemented through source terms. In the first stage, an equivalent thermal conductivity method was used to solve the vapor chamber as a conduction-only model. In the second stage, the temperature field obtained from the first stage was used as the initial condition, and the continuity, momentum, and energy equations were solved to obtain the converged thermal and flow fields. The thermal-hydraulic effects of the support columns were then investigated. Finally, the proposed method was compared with a conventional transient flow method to evaluate its reliability and computational efficiency.

2. Model description

In this section, the authors described the computational domain, modelling assumptions, and governing equations used in the study.

2.1. Structure of the vapor chamber

Following the work of Rahmatullah et al., the authors configured the computational domain as shown in Fig. 1 and divided it into three main regions: the solid enclosure, the liquid-saturated wick region, and the vapor core (Rahmatullah and Wen 2023). Only one quarter of the vapor chamber was modelled. The side, front, and top views of the computational domain were shown in Figs. 1(a), 1(b), and 1(c), respectively. The quarter-domain dimensions were 73.6 mm × 38.6 mm × 4 mm. The enclosure walls were made of copper. The wick and support columns were modelled as porous media with copper as the solid matrix and water as the working fluid, while the vapor core contained water vapor.

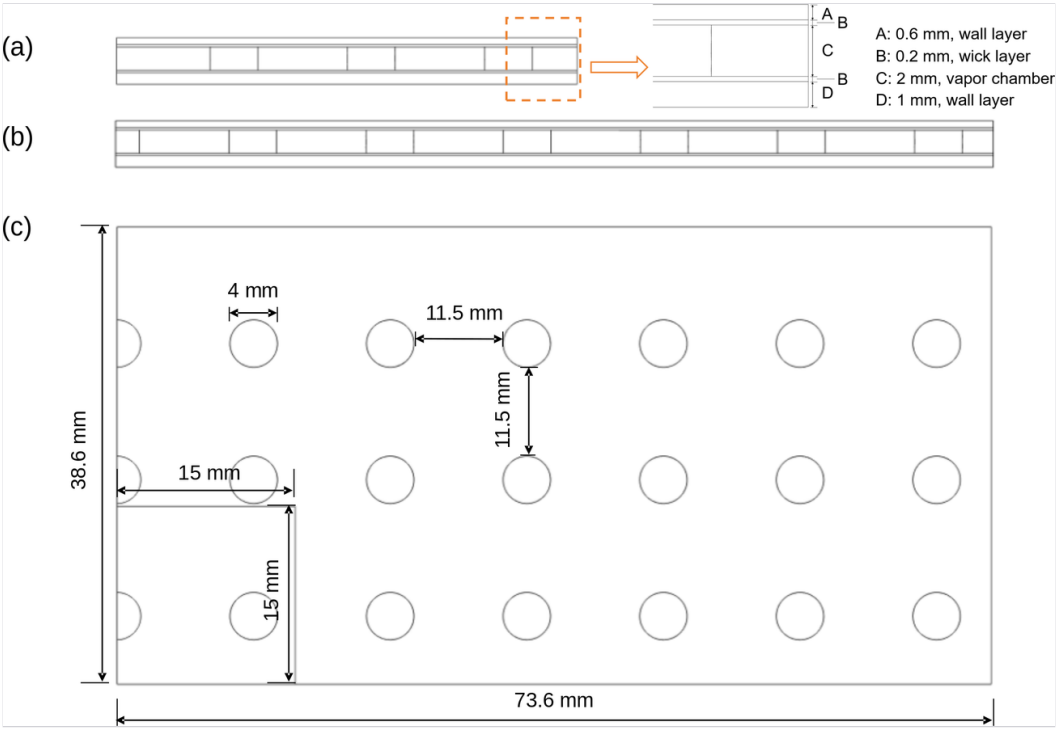

Figure 1. Quarter-domain schematic of the vapor chamber: (a) side view; (b) front view; (c) top view.

Following previous studies (Jiang *et al.* 2025), the following assumptions were adopted to simplify the numerical model:

1. The governing equations were solved in the transient state.
2. The vapor chamber was assumed to operate normally with evaporation and condensation as the phase-change modes, and no dryout was assumed to occur.
3. Evaporation and condensation were assumed to occur only at the liquid-vapor interface.
4. The fluid flow was assumed to be laminar and incompressible.
5. Gravity was neglected.

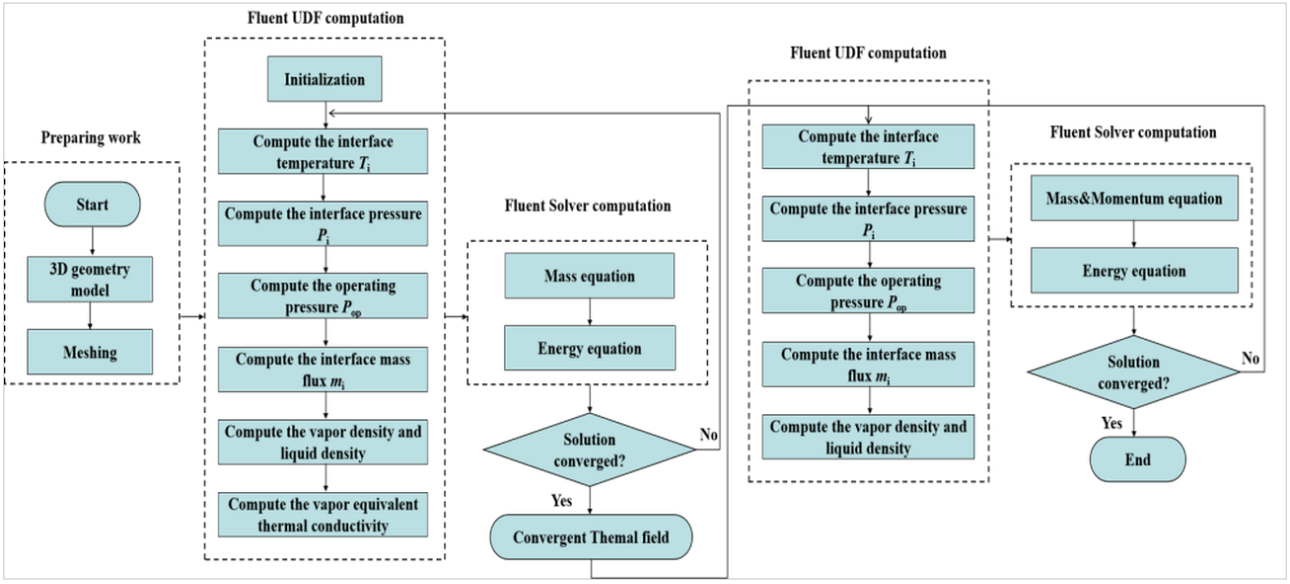

Figure 2. Computational workflow of the two-stage sequential transient numerical method.

2.2. Numerical models

Based on the above assumptions, the authors adopted a two-stage sequential transient numerical method consisting of a coarse conduction-based calculation followed by a flow calculation. The overall procedure was illustrated in Fig. 2. First, an equivalent thermal conductivity for the vapor core was derived from the conservation equations. Because the liquid velocity in the wick was very low and its contribution to convective heat transfer was limited, the wick was also treated as a solid conduction domain. In the first stage, the entire vapor chamber was therefore solved as a conduction-only domain, and the momentum equations were not required. The resulting temperature field was then used as the initial condition for the second-stage calculation, in which kinetic theory and the continuity, momentum, and energy equations were coupled to obtain the temperature, pressure, and velocity fields.

In the first stage, the vapor-core momentum equation was simplified under the assumptions described above.

$$\nabla \cdot (\rho \boldsymbol{V}\boldsymbol{V}) = -\nabla P + \mu \nabla^2 \mathbf{V} \tag{1}$$

After the inertial terms and the through-thickness velocity had been neglected, and because the vapor-core thickness was much smaller than the in-plane dimensions, the momentum equations were reduced to:

$$u = \frac{1}{2\mu}\frac{\partial p}{\partial x}(z-a)(z-b) \tag{2}$$

$$v = \frac{1}{2\mu}\frac{\partial p}{\partial y}(z-a)(z-b) \tag{3}$$

Where:

- μ = dynamic viscosity (Pa·s).
- a, b = the vertical coordinate of the cell (m).

The Clausius-Clapeyron relation was combined with the ideal-gas equation to obtain:

$$\frac{dP}{dT} = \frac{h_{fg}P_v}{R_g T_v^2} \tag{4}$$

The mass flow rates were then expressed as:

$$m_x = \rho_v A_{cell} u = \frac{P_v \rho_v A_{cell} h_{fg}}{2\mu_v R_g T_v^2}\frac{\partial T}{\partial x}(z-a)(z-b) \tag{5}$$

$$m_y = \rho_v A_{cell} v = \frac{P_v \rho_v A_{cell} h_{fg}}{2\mu_v R_g T_v^2}\frac{\partial T}{\partial y}(z-a)(z-b) \tag{6}$$

Where:

- ρ_v = the density of gas (kg/m^3).
- h_{fg} = latent heat of vaporization (J/kg).
- A_{cell} = the cross-sectional area (m^2).
- R_g = gas constant (J/kg·K).

The vapor-core energy equation was written as:

$$\nabla \cdot \left((\rho C \mathbf{V})_v T \right) = k_v \nabla^2 T \tag{7}$$

For the equivalent conduction-only model, the energy equation in the vapor core was written as:

$$k_e \nabla^2 T = 0 \tag{8}$$

Where:

- C = specific heat capacity (J/kg·K).
- k = thermal conductivity (W/m·K); the subscripts "v" and "e" denoted vapor and equivalent quantities, respectively.

Combining Equations 5-8 yielded the local equivalent thermal conductivity:

$$k_e(z) = \frac{P_v \rho_v h_{fg} C_p}{2 \mu_v R_g T_v} (z - a)(z - b) \tag{9}$$

The thickness-averaged equivalent thermal conductivity in the vapor core was expressed as:

$$\overline{k_e} = \frac{P_v \rho_v h_{fg} C_p}{12 \mu_v R_g T_v} t_v^2 \tag{10}$$

The vapor-density variation in the vapor core was updated using the ideal-gas law:

$$\rho = \frac{P_{op}}{R_g T} \tag{11}$$

Where:

- P_{op} = the operating pressure (Pa).

The operating pressure, which characterised the pressure level associated with an increase or decrease in vapor mass in the vapor core, was calculated as follows:

$$P_{op} = \frac{m_v - \Delta t \sum_i m_i}{\frac{1}{R_g} \sum_v \frac{V_{cell}}{T}} \tag{12}$$

Where:

- m_v = mass (kg).
- Δt = time step (s).
- V_{cell} = volume of the cell (m^3).

The mean liquid-density change caused by pressurisation was calculated as follows:

$$\rho_l = \frac{m_l - \Delta t \sum_i m_i}{\varepsilon V_w} \tag{13}$$

The interface temperature Ti was calculated from local energy conservation at the wick-vapor interface and was given by:

$$-k_{eff}\frac{\partial T}{\partial z} + m_i C_l T_i = -k_v \frac{\partial T}{\partial z} + m_i C_v T_i + m_i h_{fg} \tag{14}$$

The interfacial pressure was obtained from the Clausius-Clapeyron relation:

$$\frac{R_g}{h_{fg}} \ln \frac{P_i}{P_0} = \frac{1}{T_0} - \frac{1}{T_i} \tag{15}$$

The evaporation/condensation mass-transfer rate at the liquid-vapor interface was calculated using kinetic theory:

$$m_i = \left(\frac{2\sigma}{2-\sigma}\right)\frac{A_{interface}}{\sqrt{2\pi R_g}}\left(\frac{P_v}{T_v^{1/2}} - \frac{P_i}{T_i^{1/2}}\right) \tag{16}$$

Where:

- ε = porosity.
- σ = the accommodation coefficient.
- $A_{interface}$ = the cross-sectional area of the gas-liquid interface (m^2).

Previous studies had reported accommodation coefficients for water at low pressures ranging from 0.028 to 0.15 (Badam *et al.* 2007). The selected accommodation coefficient affected the thermal resistance of the liquid-vapor interface in a vapor chamber and therefore had to be determined carefully from experimental evidence. In the present study, a value of 0.02 was adopted. The evaporation/condensation mass flux at the liquid-vapor interface was assumed to be normal to the interface.

The continuity, momentum, and energy equations were solved in the vapor core and wick region to obtain the temperature, pressure, and velocity fields, as given in Equations 17-19.

$$\varepsilon\frac{\partial \rho}{\partial t} + \nabla \cdot \rho \mathbf{V} = 0 \tag{17}$$

$$\frac{\partial(\rho \mathbf{V})}{\partial t} + \nabla \cdot (\rho \boldsymbol{V}\boldsymbol{V}) = -\varepsilon \nabla P + \mu \nabla^2 \mathbf{V} - \varphi \frac{\mu \varepsilon}{K}\mathbf{V} - \varphi \frac{C_E \varepsilon}{K^{1/2}}\rho|\mathbf{V}|\mathbf{V} \tag{18}$$

$$\frac{\partial((\rho C)_m T)}{\partial t} + \nabla \cdot (\rho C \mathbf{V} T) = k_{eff} \nabla^2 T \tag{19}$$

The permeability K and inertial resistance factor IC were obtained from the Ergun equation.

$$K = \frac{D^2}{150} \frac{\varphi^3}{(1-\varphi)^2} \tag{20}$$

$$I_C = \frac{3.5}{D} \frac{(1-\varphi)}{\varphi^3} \tag{21}$$

Where:

- K = permeability (m^2).
- I_c = inertial resistance factor (m^{-1}).

In the energy equation, the effective volumetric heat capacity took different values in the solid, wick, and vapor-core regions.

Solid region

$$(\rho C)_m = (\rho C)_s \tag{22}$$

Wick region

$$(\rho C)_m = \varepsilon(\rho C)_l + (1-\varepsilon)(\rho C)_s \tag{23}$$

Vapor core region

$$(\rho C)_m = (\rho C)_v \tag{24}$$

The quantity appearing on the right-hand side of the energy equation was the effective thermal conductivity and was calculated as follows:

$$k_{eff} = \varepsilon k_l + (1-\varepsilon) k_s \tag{25}$$

The boundary conditions were specified as follows:

Heat source region

$$-k_s \frac{\partial T}{\partial n} = q \tag{26}$$

Condenser region

$$-k_s \frac{\partial T}{\partial n} = h_c (T - T_c) \tag{27}$$

All other walls

$$-k_s \frac{\partial T}{\partial n} = 0 \tag{28}$$

Symmetric surface

$$\boldsymbol{V} \cdot n = \frac{\partial T}{\partial n} = 0 \tag{29}$$

2.3. Evaluation indicators

The authors evaluated vapor-chamber performance using several thermal-hydraulic responses. As a heat spreader, a vapor chamber was required to transfer heat with low thermal resistance so that the heat generated by electronic devices could be dissipated rapidly and a low operating temperature could be maintained. The thermal resistance of the vapor chamber was evaluated by:

$$R_{th} = \frac{T_{h,avg} - T_{c,avg}}{Q} \tag{30}$$

Where:

- $T_{h,avg}$, $T_{c,avg}$ = the average temperature of the heating area and cooling area (K).
- Q = heat input (W).

Temperature uniformity was used as an indicator of flat-heat-pipe performance. A well-performing vapor chamber was expected to maintain a small temperature gradient across the condenser wall. A lower TU value therefore indicated better temperature uniformity.

$$TU = \frac{T_{c,max} - T_{c,min}}{T_{c,max}} \tag{31}$$

3. Results and discussion

In this section, the authors first validated the numerical model and then analysed the heat-transfer and hydraulic performance of vapor chambers with different support-column configurations.

3.1. Validation of numerical model

The model was first meshed for the numerical simulations. The calculation results obtained with total element numbers ranging from 226,238 to 2,832,520 were compared. The results were listed in Table 1. When the element number reached 952,393, the predicted temperatures were already close to those obtained with 2,238,850 and 2,832,520 elements. The mesh containing 2,238,850 elements was selected for the subsequent calculations.

Table 1. Grid-independence results.

	Case 1	Case 2	Case 3	Case 4
Total number of elements	226238	952393	2238850	2832520
$T_{c,ave}$/K	306.5	308.6	308.4	308.4
$T_{h,ave}$/K	311.3	313.5	313.2	313.2

To validate the accuracy of the numerical approach proposed in the present work, the authors compared the numerical predictions with the experimental data reported by Rahmatullah and Wen

(2023). The comparison was presented in Fig. 3. Overall, the simulation results agreed well with the experimental data.

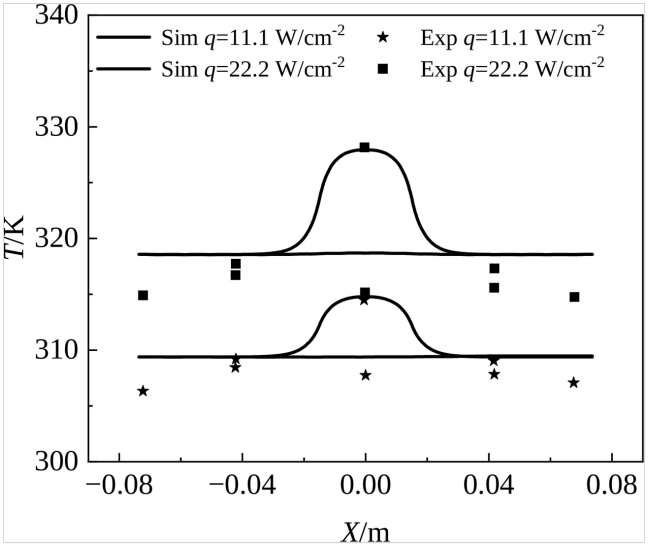

Figure 3. Comparison between numerical and experimental temperatures.

3.2. Thermal-hydraulic performance of VCs with different column numbers

Figures 4 and 5 presented a representative case in which both the transverse and longitudinal support-column pitches were 11.5 mm, corresponding to a total of 78 support columns. The temperature contours on the z = 2.2 mm plane within the vapor core were presented in Fig. 4(a). The maximum temperature of 312.8 K occurred in the heating region, whereas the minimum temperature of 308.6 K appeared near the edge in the x direction. The temperature inside the support columns was lower than that of the surrounding vapor, and a lower-temperature region was observed downstream of the columns relative to the heating region. The temperature contours on the y = 0 mm plane were presented in Fig. 4(b), where the maximum and minimum temperatures were 313.6 K and 308.4 K, respectively. The resulting temperature difference was close to 5 K and was therefore non-negligible. In addition, the temperature gradient in the z direction was clearly larger than those in the in-plane directions. These results indicated that, for a vapor chamber with fixed length and width, sufficient vapor-core thickness had to be maintained because an excessively thin vapor core could impair the heat-transport capability.

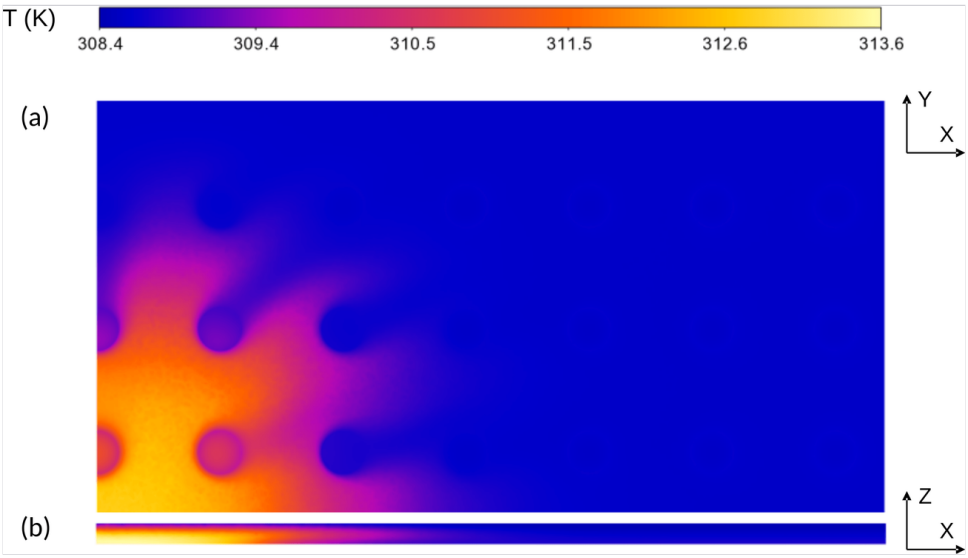

Figure 4. Temperature contours: (a) xoy plane (z = 2.2 mm); (b) zox plane of the vapor core.

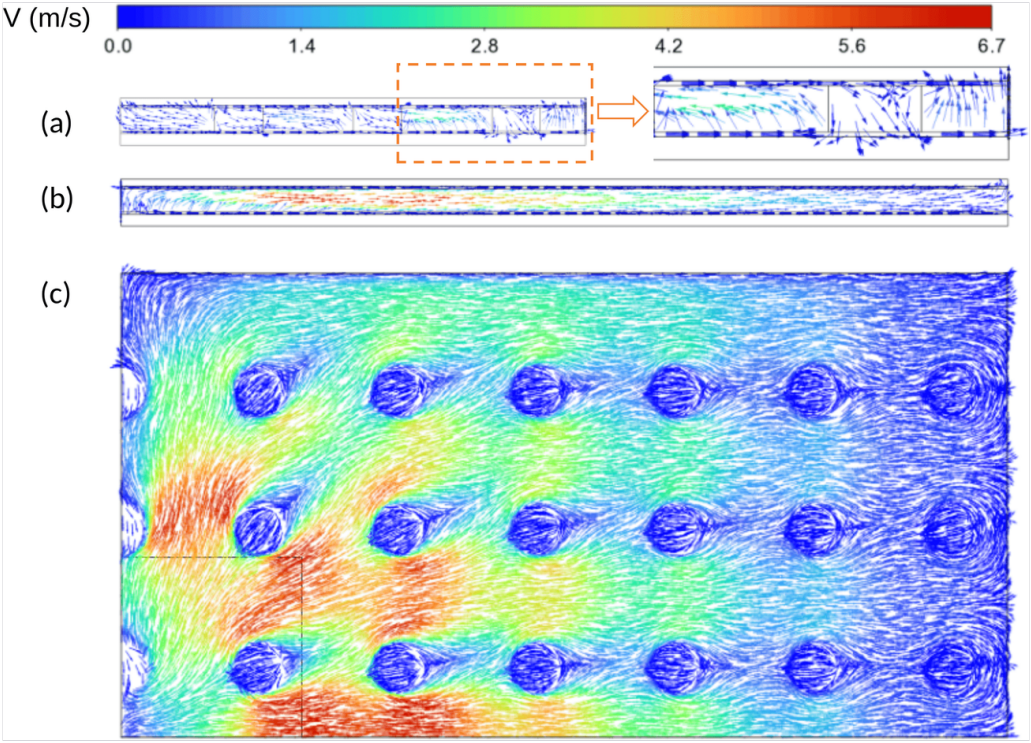

Figure 5. Velocity-vector distributions: (a) side view; (b) front view; (c) top view.

Velocity-vector distributions for the case with transverse and longitudinal support-column pitches of 11.5 mm were presented in Fig. 5. The maximum vapor velocity in the vapor core was 6.7 m/s, whereas the maximum liquid velocity in the wick and support columns was only 2×10^{-3} m/s. This large difference was mainly attributed to the substantial density difference between vapor and liquid and to the higher flow resistance in the porous media. Figure 5(a) presented a side view of the vapor chamber. The support columns provided liquid-return paths from the condenser region to the heating region and therefore played an important role in stable vapor-chamber operation. The enlarged view further indicated that, near the heating region, vapor at the support-column/vapor-core interface flowed from the support column into the vapor core, which indicated that evaporation also occurred at the column interface and contributed to heat transport. The front and top views were presented in Figs. 5(b) and 5(c), respectively. In Fig. 5(b), the maximum vapor velocity generated from the heating region occurred near the edge rather than at the centre. This occurred because evaporation took place over the entire heated area, so the vapor flow rate increased towards the edge; in addition, the support columns locally reduced the available vapor-flow area. As illustrated in Figs. 4(b) and 5(c), the vapor streamlines bent around the support columns and formed low-velocity wake regions downstream of the columns. These regions were cooler than the surrounding vapor and were associated with vortex and recirculation effects induced by the obstruction of the support columns. The overall circulation process was also identified from Fig. 5: the liquid first evaporated in the heating region and became vapor, after which the vapor flowed away from the heating region. Vapor moving towards the condenser condensed at the wick-vapor interface, while vapor flowing laterally also condensed at the column/vapor interface. The condensed liquid then returned to the heating region through the wick and support columns and evaporated again.

Temperature contours for vapor chambers with different transverse and longitudinal support-column pitches were compared in Fig. 6 at a heat flux of 22.2 W/cm^2. The yz- and zx-symmetry planes were presented for the different cases, and a pronounced temperature change was visible across the liquid-vapor interfaces. On the yz-symmetry plane, the through-thickness temperature difference in the vapor core was much smaller than that across the support columns. This difference occurred

because the effective thermal conductivity of the support-column region was lower than that of the vapor core, which resulted in higher thermal resistance and more limited heat transfer through the columns. The temperature field remained relatively uniform in the in-plane directions, which demonstrated the strong heat-spreading capability of the vapor chamber. Among the cases considered, the configuration with a transverse pitch of 8 mm and a longitudinal pitch of 8.4 mm exhibited a higher heating-surface temperature, and the overall vapor-chamber temperature was also higher than those in the other cases. These results suggested that an excessively dense support-column arrangement could deteriorate heat-transfer performance.

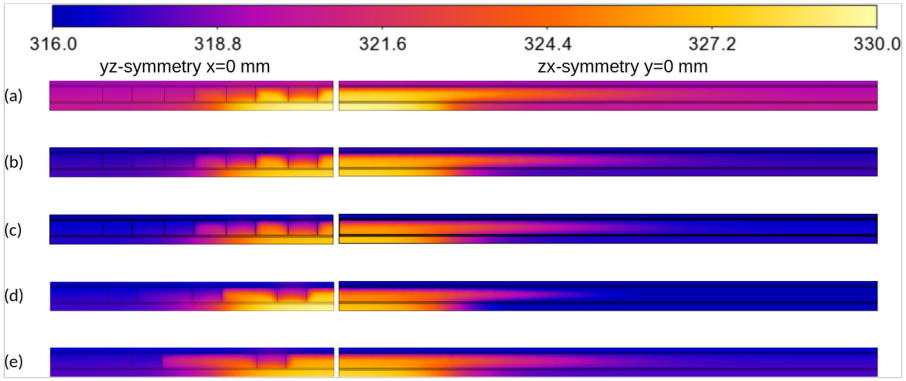

Figure 6. Temperature contours at 200 W (22.2 W/cm²) on the xz- and yz-symmetry planes for different transverse and longitudinal pitches. (a) Pitch 8 mm × 8.4 mm; (b) pitch 11.5 mm × 8.4 mm; (c) pitch 16 mm × 8.4 mm; (d) pitch 11.5 mm × 11.5 mm; (e) pitch 17 mm × 11.5 mm.

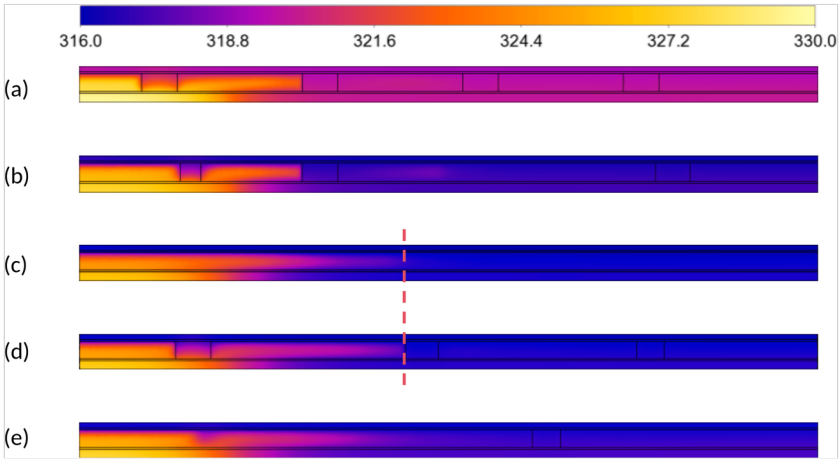

Figure 7. Temperature contours at 200 W (22.2 W/cm²) along the diagonal section.

Temperature contours along the diagonal section of vapor chambers with different transverse and longitudinal support-column pitches were compared in Fig. 7 at a heat flux of 22.2 W/cm², corresponding to the cases in Figs. 6(a)-6(e). The diagonal direction represented the longest vapor-flow path in the chamber. The overall temperature in case (a) was higher than those in the other cases, which was consistent with the preceding discussion. In cases (c) and (d), the vapor-core temperature decreased rapidly along the in-plane direction and had already approached the temperature at the end of the diagonal direction in the region marked by the red dotted line. A similar trend was observed in Figs. 6(c) and 6(d). The in-plane temperature decreased rapidly on the yz-symmetry plane in case (c) and on the zx-symmetry plane in case (d). The average heating-surface temperatures of cases (c) and (d) were also lower than those of the other cases. These results indicated that the in-plane temperature-gradient pattern within the vapor core could be used as a qualitative indicator of heat-spreading performance. They also indicated that both excessively large and excessively small numbers of support columns could reduce heat-spreading performance.

Velocity-vector distributions on the z = 2.2 mm plane at a heating power of 200 W were compared in Fig. 8 for vapor chambers with different transverse and longitudinal support-column pitches. Near the heating region, case (c) exhibited a large difference between vapor velocities in the transverse and longitudinal directions, whereas case (d) showed the smallest directional difference. In case (a), although the transverse and longitudinal pitches were similar, the velocity in the longitudinal direction was still higher. These results indicated that a large difference between transverse and longitudinal pitches could lead to pronounced directional differences in vapor velocity. However, equal pitches did not necessarily minimise the velocity anisotropy, possibly because of the aspect ratio of the vapor chamber. In addition, the pitches affected the orientation of the low-velocity wake regions downstream of the columns, particularly near the edge of the heating region, which could in turn influence the temperature distribution.

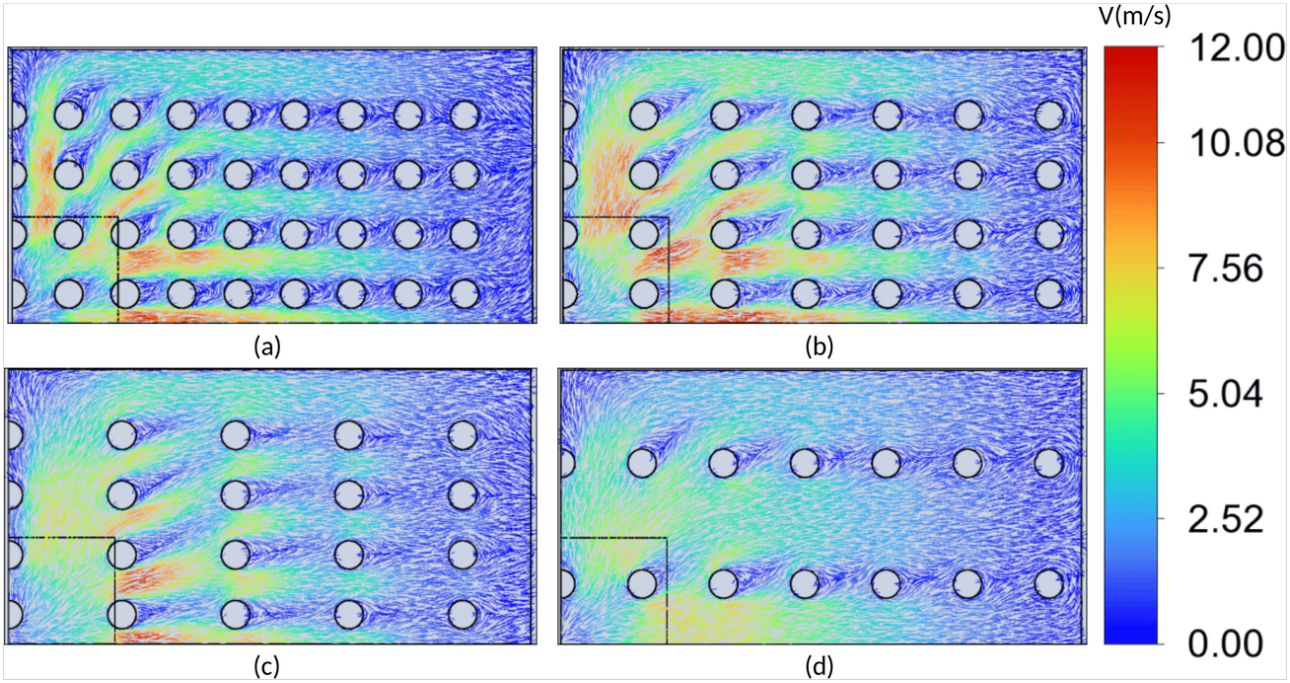

Figure 8. Velocity-vector distributions at 200 W (22.2 W/cm²) on the z = 2.2 mm plane for different transverse and longitudinal pitches. (a) Pitch 8 mm × 8.4 mm; (b) pitch 11.5 mm × 8.4 mm; (c) pitch 16 mm × 8.4 mm; (d) pitch 11.5 mm × 17 mm.

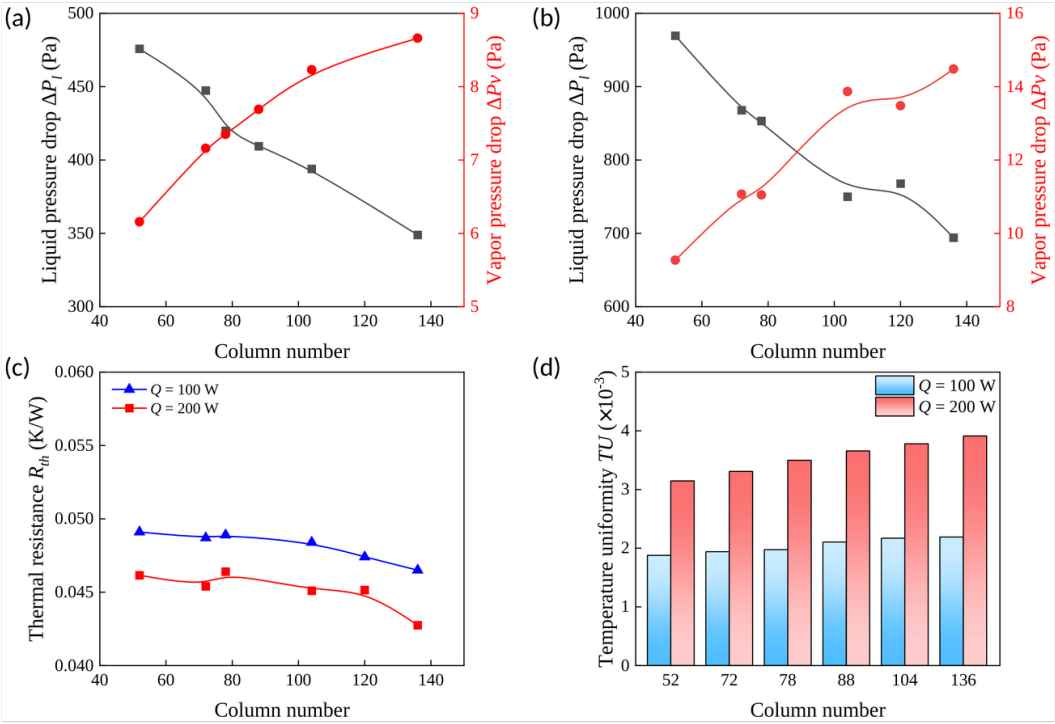

Figure 9. Effect of the number of support columns on the thermal-hydraulic performance of the vapor chambers.

The effects of support-column number on vapor-chamber performance were presented in Fig. 9. The hydraulic performance at heat inputs of 100 W and 200 W was presented in Figs. 9(a) and 9(b), respectively. For N = 40-140, the liquid pressure drop decreased as the number of support columns increased, whereas the vapor pressure drop increased. Increasing the number of support columns provided additional return paths for the condensate, but it also increased the contact area between the columns and the vapor and obstructed vapor flow, thereby increasing the vapor-flow resistance. The variation in vapor-chamber thermal resistance with support-column number was presented in Fig. 9(c). The thermal resistance decreased slightly as the number of columns increased and was lower at the higher heat input. At Q = 100 W, the thermal resistance decreased from 0.0491 K/W to 0.0465 K/W, corresponding to a reduction of 5.3%. At Q = 200 W, it decreased from 0.0462 K/W to 0.0428 K/W, corresponding to a reduction of 7.4%. Increasing the number of support columns therefore reduced the overall thermal resistance, and the benefit was more pronounced at the higher heat load. As presented in Fig. 9(d), temperature uniformity deteriorated as the number of support columns increased at both heat inputs. Figures 9(c) and 9(d) therefore revealed a trade-off: additional columns reduced the mean temperature difference between the heating and cooling surfaces, but they also redistributed the local heat-transfer paths and vapor flow, thereby reducing the overall temperature uniformity.

3.3. Methodology comparison

The proposed two-stage sequential transient numerical method was compared with a conventional transient flow calculation for a vapor chamber initialised at 300 K, as presented in Fig. 10. The computational times were compared in Fig. 10(a): the conventional flow calculation required 9,907 s, whereas the two-stage method required 5,381 s. The proposed strategy therefore reduced the computational time by 45.7%, corresponding to a speedup of approximately 1.84 times. In addition to reducing the computational cost, the improved initial temperature field enhanced the numerical robustness of the subsequent flow calculation. The predicted results from the two approaches were compared in Fig. 10(b), and the nearly identical solutions demonstrated the reliability of the two-stage method.

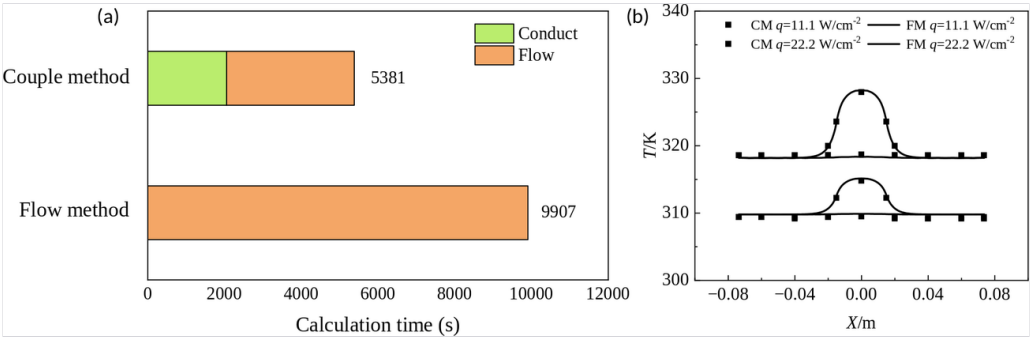

Figure 10. Comparison of the proposed method with the conventional flow method.

4. Conclusion

In this study, the authors developed a new transient numerical method for vapor-chamber simulation. The vapor- and liquid-flow characteristics and temperature distributions during stable operation were analysed. The effects of support-column spacing and number on the flow field, temperature field, and thermal-hydraulic performance were investigated. The main conclusions were as follows.

1. The proposed method reduced the computational cost by 45.7%, corresponding to a speedup of approximately 1.84 times, while producing negligible deviations in the predicted temperatures. It also provided improved initialization and computational robustness.
2. Support-column pitch significantly influenced the vapor-flow and thermal fields near the heater. The columns provided additional liquid-return channels but also obstructed vapor flow, and smaller spacing resulted in higher local vapor velocities. Low-velocity, low-temperature wake regions formed downstream of the columns, and their orientation depended on the transverse and longitudinal pitches.
3. Increasing the number of support columns increased the vapor pressure drop, reduced the liquid pressure drop and the overall pressure drop, and lowered the thermal resistance, with a more pronounced reduction at the higher heating power. However, a greater number of columns degraded the temperature uniformity, and this non-uniformity became more pronounced at the higher heat load.

Declarations

Author contributions. Haojiang Ran: Conceptualization, Methodology, Investigation, Formal analysis, Data curation, Writing (original draft), Writing (review and editing), Visualization, Validation, Software. Xinyi Wang: Formal analysis, Visualization. Lu Wang: Visualization. Tiexiao Xu: Visualization. Zhen Li: Supervision, Project administration, Resources, Funding acquisition.

Funding. This research received no specific funding.

Conflicts of interest. None

Data availability. All data generated or analysed during this study are included in this paper.

References

Badam, V.K.; Kumar, V.; Durst, F.; Danov, K. (2007) 'Experimental and theoretical investigations on interfacial temperature jumps during evaporation', *Experimental Thermal and Fluid Science*, 32(1), pp. 276-292. Available at: https://doi.org/10.1016/j.expthermflusci.2007.04.006

Jiang, Hongpeng; Wang, Xiaoliang; Xu, Zhiming; Qi, Hong; Shan, Debin; Guo, Bin; Xu, Jie (2025) 'Numerical analysis of support column manipulation for efficient heat transfer in vapor chambers', *International Journal of Heat and Mass Transfer*, 253, pp. 127520. Available at: https://doi.org/10.1016/j.ijheatmasstransfer.2025.127520

Koito, Yasushi; Imura, Hideaki; Mochizuki, Masataka; Saito, Yuji; Torii, Shuichi (2006) 'Numerical analysis and experimental verification on thermal fluid phenomena in a vapor chamber', *Applied Thermal Engineering*, 26(14-15), pp. 1669-1676. Available at: https://doi.org/10.1016/j.applthermaleng.2005.11.012

Prasher, Ravi S. (2003) 'A Simplified Conduction Based Modeling Scheme for Design Sensitivity Study of Thermal Solution Utilizing Heat Pipe and Vapor Chamber Technology', *Journal of Electronic Packaging*, 125(3), pp. 378-385. Available at: https://doi.org/10.1115/1.1602479

Rahmatullah, Yusuf; Wen, Tsrong-Yi (2023) 'Lee model based numerical scheme for steady vapor chamber simulations', *International Journal of Heat and Mass Transfer*, 201, pp. 123636. Available at: https://doi.org/10.1016/j.ijheatmasstransfer.2022.123636

Vadakkan, Unnikrishnan; Murthy, Jayathi Y.; Garimella, Suresh V. (2003) 'Transient Analysis of Flat Heat Pipes', *Proceedings of the ASME 2003 Summer Heat Transfer Conference (HT2003), Las Vegas, Volume 3*. ASMEDC, pp. 507-517. Available at: https://doi.org/10.1115/ht2003-47349

HOW TO CITE THIS PAPER

Ran, H., Wang, X., Wang, L., Xu, T. and Li, Z. (2026). Numerical analysis of support columns in vapor chambers. In: *Proceedings of the 22nd International Conference on Sustainable Energy Technologies (SET2026)*, Kuala Lumpur, Malaysia, 13 to 15 August 2026. Caravel Press, pp. 166–180. ISBN 978-1-995850-00-9. ISSN 2978-4387. https://doi.org/10.65582/set.2026.014

COPYRIGHT AND LICENCE

© 2026 The Author(s). This is an open access paper distributed under the terms of the Creative Commons Attribution (CC BY 4.0) licence, which permits unrestricted use, distribution and reproduction in any medium, provided the original work is properly cited.

WSSET World Society of Sustainable Energy Technologies Organised by the World Society of Sustainable Energy Technologies. Published by Caravel Press.